

# Unsupervised Cell Identification on Multidimensional X-Ray Fluorescence Datasets

Siwei Wang,<sup>a,\*</sup> Jesse Ward,<sup>b</sup> Sven Leyffer,<sup>a</sup> Stefan M. Wild,<sup>a</sup> Chris Jacobsen,<sup>b,c,d</sup> and Stefan Vogt<sup>b</sup>

<sup>a</sup>Mathematics & Computer Science Division, Argonne National Laboratory, 9700 S. Cass Ave. Argonne, IL 60439 USA, <sup>b</sup>Advanced Photon Source, Argonne National Laboratory, 9700 S. Cass Ave. Argonne, IL 60439, <sup>c</sup>Department of Physics & Astronomy, Northwestern University, 2145 Sheridan Rd. Evanston, IL 60208, and <sup>d</sup>Chemistry of Life Processes Institute, Northwestern University, 2170 Campus Dr. Evanston, IL 60208. E-mail: siweiw@mcs.anl.gov

We introduce a novel approach to locate, identify, and refine positions and whole areas of cell structures based on elemental contents measured by X-ray fluorescence microscopy. We show that by initializing with only a handful of prototypical cell regions, this approach can obtain consistent cell populations, even when cells are partially overlapping, without training by explicit annotation. It is robust both to different measurements on the same sample and to different initializations. This effort provides a versatile framework to identify targeted cellular structures from datasets too complex for manual analysis, like most X-ray fluorescence microscopy data. We also discuss possible future extensions.

## 1. Introduction

X-ray fluorescence microscopy (XFM) provides submicrometer-resolution information on the localization and quantity of all but the lightest elements. For studies of micrometer-thick biological specimens, it provides this information with lowest dose for a given elemental sensitivity (Kirz, 1980), so that it has emerged as a powerful method for studies in biology and medicine (Paunesku *et al.*, 2006). By using high-resolution optics such as Fresnel zone plates, multi-keV X-rays are focused to a small spot through which the specimen is scanned. Absorption of these X-rays leads to the ejection of core shell electrons, and photons at characteristic elemental fluorescence energies are emitted as outer shell electrons fill the core shell vacancies (a competing process of emission of Auger electrons is small for elements with atomic number greater than about 15 (Krause, 1979)). An energy-dispersive detector is used to record the energy of individual fluorescence photons, thus providing information on elemental content at that pixel location. These multispectral data typically contain 1000 or more energy channels per pixel, which in our case have been analyzed to obtain concentrations of chemical elements as described in Sec. 2.

We are not the first to recognize that scientific capability for intuitive understanding is being overwhelmed by the volume and complexity of data generated in modern microscopies. In light microscopy, Swedlow *et al.* have noted that “multidimensional imaging has driven a revolution in modern biology—yet the significant data management and analysis challenges presented by these new complex datasets remain largely unsolved” (Swedlow *et al.*, 2009). In recognition of these challenges, we have already made some progress. Members of our team have written

a program called MAPS (Vogt, 2003) for quantification and fitting of multidimensional X-ray fluorescence images and a cluster analysis-based program PCA\_GUI for classification and analysis in soft X-ray spectromicroscopy (Lerotic *et al.*, 2004; Lerotic *et al.*, 2005) (this program has migrated to an open-source project at [code.google.com/p/spectromicroscopy](http://code.google.com/p/spectromicroscopy)). MAPS carries out the analysis required to go from per-pixel fluorescence spectra to per-pixel elemental concentration (described in Sec. 2), along with analysis through the manual generation of spatial regions of interest; enhancements to include principal component analysis and clustering are promising but not yet reliable enough for unsupervised analysis of large datasets. PCA\_GUI provides cluster analysis but suffers from negative, unphysical weightings in some analyses (now being addressed through the use of non-negative matrix factorization). These efforts are not yet as advanced as clustering and machine-learning analysis implemented in optical microscopy (Ljosa & Carpenter, 2009) or hyperspectral analysis used in aircraft and satellite imaging (Plaza *et al.*, 2004). Our goal here is to provide classification from X-ray fluorescence spectra with no subsequent higher-level processing required, so as to greatly enhance how we approach and understand the rich data sets generated from X-ray fluorescence excitation in electron, proton, and X-ray excitation microscopy methods.

Recent developments in medical imaging have employed various object recognition methods to identify cellular structures automatically, such as whole cells using phase-contrast microscopy (Tao *et al.*, 2007), cell nuclei using 3D microscopy video (Aydin *et al.*, 2010; Lin *et al.*, 2003), and vesicles in time-lapse microscopy (Cortés & Amit, 2008). These approaches employ expert knowledge on gray-level or texture difference between the targeted cellular structures and the pictured background, and they model these structures, or the groups of pixels embedded in them, as graph nodes or data items. With these prototypes in mind, they capture the cellular structural information within common pattern recognition frameworks such as graph/random fields (Al-Kofahi *et al.*, 2010), Bayesian classification (Yin *et al.*, 2010), support vector machines (Wang *et al.*, 2007; Aydin *et al.*, 2010; Kasson *et al.*, 2005), and neural networks.

Most of the previous work originated from one of two basic types of machine learning/computer vision approaches. The first is formulating energy functionals that can be solved by combinatorial optimization techniques, such as graph cuts (Wolz *et al.*, 2010; Bergeest & Rohr, 2011), dynamic programming (McCullough *et al.*, 2008; Arteta *et al.*, 2012), and Potts-model-based Markovian random fields (Russell *et al.*, 2007). The second type includes the family of differential methods such as level set (Lin *et al.*, 2003) and active contour (McCullough *et al.*, 2008) methods. Both types of methods were developed based on bright-field, confocal, and fluorescence images where one typically has only a few intensity channels; our approach is aimed at addressing a larger number of channels since x-ray fluorescence can detect a large number of chemical elements simultaneously.

We propose here a novel approach to locate, identify, and refine positions and areas of cellular structures based on their characteristic elemental distributions. To demonstrate the ability of this approach to identify cells and distinguish their types, we apply it to a dataset of three intermixed cell types. We begin by using MAPS to reduce the acquired fluorescence spectra into quantitative concentrations of 9 chemical elements. As input parameters for subsequent analysis, the approach accepts lower bounds, averages, and standard devia-

tions of cell types from a few hand-drawn regions of interest (ROIs) for each type. (These hand-drawn ROIs can in the future be replaced by representative contents from other reference data or learned automatically.) The approach uses a generalized likelihood ratio test to model multiple overlapping cells, which is common for 2D images of biological samples; to the best of our knowledge, several previous methods that claimed global optimality can handle only samples that are at most touching at the boundaries (Bergeest & Rohr, 2012). In contrast to previous approaches that are based on manual annotations (Kasson *et al.*, 2005; Lin *et al.*, 2003; Wang *et al.*, 2007) and heavily rely on availability of a large training set, our approach is able to identify cells even in cases where manual annotation is limited or not available.

The paper is organized as follows. In Section 2, we discuss sample preparation, data acquisition, and the datasets we employed in evaluating the consistency and robustness of this approach. In Section 3, we provide a high-level description of the components of our problem and approach. In Section 4 we introduce the four underlying procedures in detail: preprocessing, estimating group configuration, boundary delineation, and pixel refinement. Currently, each procedure can be viewed as solving an optimization problem, the solution of which is then passed as an input to the next procedure. However, this approach can be modified such that the output of the last step can serve as the input to the first step. We report our resulting element distributions in Section 5 and demonstrate that this approach generates robust statistics of cell populations with respect to initial parameters. Since this cell identification approach is in early stages of development, many opportunities for improvement remain, some of which are discussed in Section 7. We also comment on the benefit of applying this approach to XFM data analysis.

## 2. Sample and Data

We prepared a test sample set (shown in Fig. 1) with three distinct cell types: red blood cells (rabbit erythrocytes), common yeast (*Saccharomyces cerevisiae*), and algae (*Chlamydomonas reinhardtii*) in order to evaluate this cell identification approach. These cell types were chosen on the basis of both availability and expected differences in elemental content. For example, red blood cells were expected to contain relatively more iron than other cell types because of the presence of heme iron in hemoglobin (Hawkins *et al.*, 1954), and algae were expected to contain relatively greater manganese levels because of the presence of manganese in photosystem II (Dismukes, 1986).

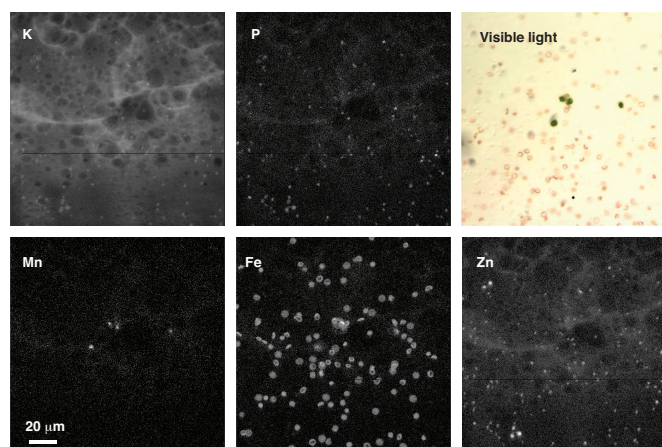


**Figure 1**

Data used for subsequent analysis. A mixture of three cell types was prepared, as shown in the visible light micrograph: red blood cells, algae, and yeast. The maps of particular elements (K, P, Mn, Fe, and Zn) obtained from X-ray fluorescence images hint at the characteristics of the different cell types: Mn is prevalent in algae and Fe in red blood cells, while Zn and P are indicative of yeast cells. The visible light micrograph was acquired at one focal plane and thus does not show all cells; separate slight distortions in relative cell positions between the X-ray fluorescence maps and the visible light micrograph were not adjusted for.

Washed and pooled rabbit red blood cells at 10% hematocrit were purchased from Lampire Biological Laboratories (Pipersville, PA). A 1 mL volume sample was drawn and centrifuged for 10 minutes at 600 g. The supernatant was discarded, and cells were resuspended in a solution of 200 mM sucrose and 10 mM PIPES (Good *et al.*, 1966), both from Sigma-Aldrich (St. Louis, MO). Yeast cells were inoculated in 2.5 mL of sterile YPD media (Lundblad & Struhl, 2001) and grown in a shaking incubator at 30°C and 300 rpm for 24 hours. A 1 mL volume sample was drawn and centrifuged for 10 minutes at 600 g. The supernatant was discarded, and cells were resuspended in a solution of 200 mM sucrose and 10 mM PIPES.

Algae cells were provided by Qiaoling Jin (Argonne). The wild type strain of *Chlamydomonas reinhardtii* was purchased from ATCC (Manassas, VA) and grown mixotrophically in TAP medium (Gorman & Levine, 1965) on a rotary shaker (120 rpm) at 25°C and in the presence of  $\approx 100 \mu\text{mol photons m}^{-2} \text{ s}^{-1}$  of photosynthetically active light. A 1 mL volume sample was drawn and centrifuged for 2 minutes at 600 g. The supernatant was discarded, and cells were resuspended in a solution of 200 mM sucrose and 10 mM PIPES. Equal volumes of red blood cells, yeast cells, and algae cells were suspended in 200 mM sucrose and 10 mM PIPES and then mixed together. A 2  $\mu\text{L}$  volume was spotted onto a 200 nm thick silicon nitride window (Silson Ltd., Northampton, UK) and allowed to air dry overnight.

X-ray fluorescence imaging was performed at beamline 2-ID-E at the Advanced Photon Source at Argonne. Undulator-produced X-rays at 10 keV incident energy were focused to a spot size of 0.8  $\mu\text{m}$  by 0.8  $\mu\text{m}$  using Fresnel zone plate optics (Xradia, Inc., Pleasanton, CA). Samples were raster-scanned through the X-ray beam in fly-scanning mode, covering about a  $(200 \mu\text{m})^2$  area with a pixel size  $\delta=0.3 \mu\text{m}$  in each direction,  $666 \times 667$  pixels, and an effective dwell time of 100 ms per pixel. Full fluorescence spectra were detected at each pixel using a 4-segment silicon drift detector (Vortex-ME4, Hitachi High-Technologies Science America, Northridge, CA), with each detector segment collecting a slightly different signal because

of angular variations in scattered signals, different self-absorption paths to the segment, and so on.

Every pixel in the XFM dataset originally contains the full X-ray spectra recorded from the four detector segments. These spectra were then processed by MAPS (Vogt, 2003), which involves a fitting procedure and calibration based on a standard with known elemental concentration to yield quantitative maps of elemental concentration in  $\mu\text{g}/\text{cm}^2$ . Those quantitative maps for the elements P, S, Cl, K, Ca, Mn, Fe, and Zn provided the input data for the analysis procedures described here.

The three cell types have somewhat different sizes. We therefore introduce a lower-bound area parameter  $s_t$  per cell type for subsequent analysis: we used  $s_t=200$  pixels (or  $18 \mu\text{m}^2$ ) for red blood and algae cells, and  $s_t=30$  pixels (or  $2.7 \mu\text{m}^2$ ) for yeast cells.

### 3. Problem and Overview

We address the fundamental question ‘‘Where are the (whole) cells?’’ based on recorded elemental distributions in an XFM dataset. The goal of our approach is to identify cells of different types, while also allowing for multiple cells to overlap.

A key difficulty here is that often no manual annotation is available to serve as a reference; we know only that the total elemental contents of the whole cell areas, shape, and size of cells of a given type can be employed as salient features. We use the following two classes of expert-informed cell features to initialize this approach:

1. *Morphology*. We assume that all cells of a specific type have somewhat similar sizes and shapes.
2. *Content*. We assume that cells of a specific type have similar total content in characteristic elements, and that these characteristic elemental contents are distinct compared with cells of other types.

In the present study, we seed our analysis by per-hand identification of regions of interest (ROIs) around a few isolated cells of each type. This was appropriate for an initial study, though in the future the seeding could be done from literature values for elemental composition and area  $s_t$ .

In our case, the ROIs provide twofold information: (1) the element or combination of elements provides characteristic elemental maps that distinguish each specified cell type, and (2) the content from these ROIs is employed as representative total elemental content of these cells. We use the former information to preprocess the dataset and obtain initial guesses for the areas of putative cells. We use the latter to refine these putative cells.

The initial inputs for this approach are thus information on the morphology and content features. Preprocessing of the putative cells (Section 4.1) is done by image segmentation. We first divide pixels of the image of a given characteristic element into foreground and background components (e.g., based on their intensity).

We partition all foreground pixels into groups via the recursive min-cut algorithm (Dhillon *et al.*, 2007) and then fit a minimum-area ellipse around each of these segments as the initial guess of cell areas. Here, we tailor the partition algorithm to oversegment in order to cover actual cells with at least one group.

This oversegmentation conditions the configuration estimation procedure in Section 4.2 to focus on evaluating group configurations with potentially reduced number of cell groups. This estimation procedure determines whether merging two groups or deleting a group will represent the total content better than the current configuration. We represent the total content criteria with Gaussian distributions (specified by a mean and diagonal covariance) obtained from the given content inputs.

After we estimate the configuration of cell groups, we refine these putative cell groups by adjusting their boundaries based on a total elemental content criteria (see Section 4.3). This procedure aims at recovering pixels that are within a cell but were initially relegated to the background because of thresholding. For every boundary we obtain by this procedure, we compensate for potential smoothness discrepancies using a pixel refinement procedure (see Section 4.4). This procedure ensures that the resulting areas cover the group of pixels best for their corresponding cells.

This multistep approach is versatile and can be applied to a broad class of identification problems. The components described here can also be employed independently or combined to answer different scientific questions.

**Procedure 1:** Overview of the approach.

**Inputs:** Pixels  $P$  of an XFM dataset, cell types  $\mathcal{T}$ , characteristic element  $e_t$  and lower bound of size  $s_t$  for all  $t \in \mathcal{T}$ , means and standard deviations of representative cell contents;

**for all**  $t \in \mathcal{T}$

- Obtain foreground and background of  $e_t$ ;
- Partition foreground pixels using elemental map of  $e_t$ , such that all segments contain at most  $s_t$  pixels;
- Obtain groups  $\mathcal{G}_t$  of type  $t$  by using minimum-area ellipses to cover all individual segments;

**end for**

- Obtain groups  $\hat{\mathcal{G}}$  from initial groups  $\mathcal{G} = \cup_t \mathcal{G}_t$  by either merge or deletion;
- Delineate boundaries of all groups  $g \in \hat{\mathcal{G}}$  using both morphology and content features;
- Refine pixel boundaries of all  $g \in \hat{\mathcal{G}}$ ;

### 4. Our Approach

For a given image, we let  $P$  denote the set of pixels in the image, with each pixel indexed by a pair of (column, row) indices  $(x, y)$ . We use uppercase roman letters to denote sets of pixels and use calligraphic letters to refer to other types of sets (e.g., index sets, elements, cell types) throughout the sequel.

Let  $F$  and  $B$  denote disjoint sets of foreground and background pixels, respectively, so that  $P = F \cup B$ . We designate a *group of pixels* by  $G_g$ , where  $g \in \mathcal{G}$  denotes a group index. Groups will ultimately be used to define a cell, but we use the term ‘‘group’’ to acknowledge that, particularly in the initial steps of this approach, there may not be a one-to-one correspondence between groups and cells. The collection of all groups defines the foreground pixels as  $F = \cup_{g \in \mathcal{G}} G_g$ . Associated with each group  $G_g$  will be a set of local background pixels  $B_g$ , more formally defined in Section 4.1.2.

A *region*  $R_r$  (with  $r \in \mathcal{R}$ ) consists of pixels belonging to one or more groups and their local backgrounds. We let  $\mathcal{G}_r \subseteq \mathcal{G}$  denote the set of groups belonging to region  $R_r$  so that  $R_r = \cup_{g \in \mathcal{G}_r} (G_g \cup B_g)$ . The sets  $\mathcal{G}_r$  form a partitioning of  $\mathcal{G}$ . We denote the local background of region  $R_r$  by  $B_r$  (defined in Section 4.1.2).

For a general set of pixels  $Z$ , we define  $c_e(Z)$  to be the total content in  $Z$  of element  $e \in \mathcal{E}$ . In this paper, we limit our discussion to  $|\mathcal{E}| = 9$  elements  $\mathcal{E} = \{\text{P, S, K, Cl, Ca, Mn, Fe, Cu, Zn}\}$ . We assume that a *content map* (see Section 2) provides  $c_e(x, y)$  for each  $(x, y) \in P$  and each  $e \in \mathcal{E}$ .

Each group will have an associated type  $t \in \mathcal{T}$ ; in this paper  $\mathcal{T} = \{\text{algae, rbc, yeast}\}$ . Associated with each type  $t$  are various quantities, either provided by an expert or learned in the course of the procedures below.

Using this notation, we organize our approach as follows:

1. *Preprocessing and Image Segmentation*: Specify elemental content distributions for each cell type, identify the foreground pixels  $F$ , divide the foreground into  $|\mathcal{G}|$  possibly overlapping groups, and aggregate the groups into  $|\mathcal{R}|$  disjoint regions (Section 4.1).
2. *Estimation of Group Configuration*: Given a set of groups  $\mathcal{G}$  and a set of disjoint regions  $\mathcal{R}$ , adjust the number and areas of groups of each type within each region to best match the observed elemental contents (Section 4.2).
3. *Optimization of Group Boundaries*: Given putative cell groups in each region, determine smooth curves to serve as boundaries of the cells (Section 4.3).
4. *Local Pixel Refinement*: For the smooth boundaries in a region that do not satisfy local optimality conditions, refine each associated group so the content of its discrete set of pixels best matches the content in a cell (Section 4.4).

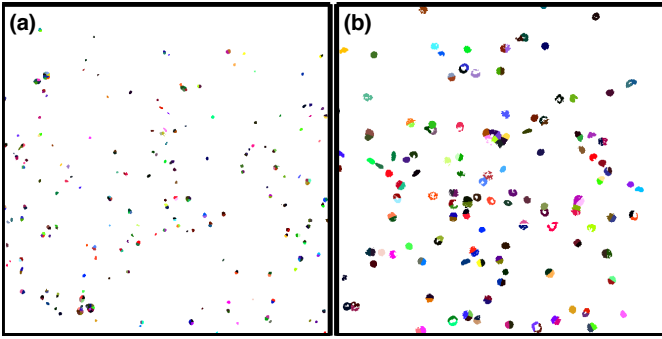


**Figure 2**  
Image segmentation result used to form the initial groups for yeast and red blood cells based on the markers Zn (a) and Fe (b), respectively. Algae cells are not shown because there are only 5 cells.

#### 4.1. Preprocessing and Image Segmentation

The first procedure is responsible for producing the representative elemental distributions, a set of initial groups  $\mathcal{G}$  and regions  $\mathcal{R}$ , and the local backgrounds for each of these groups and regions.

**4.1.1. Initial Group Formation.** We take as input the individual elemental maps and the segment area bound  $s_t$ ; for purposes of oversegmentation,  $s_t$  is taken to be the smallest cell area from the hand-selected ROI. We then perform an image segmentation using images from three characteristic elements (Mn for algae, Fe for red blood cells, and Zn for yeast). The resulting segments (shown in Fig. 4) each locate a possible area for a cell of type  $t$ .

Based on these segmentations, we form minimum-area ellipses to cover pixels belonging to the same segment. Ellipses are appropriate for the cell types considered here; more complicated shapes can also be considered. The pixels in each ellipse are used to define an initial group  $G_g$ . By construction, all groups contain a contiguous set of pixels.

**4.1.2. Region Formation and Background Content.** Knowledge of the background content is important in XFM analysis. When using energy dispersive detectors to record the fluorescence signal, there will be some contribution at all energies as a result of inelastic scattering and incomplete collection of the charge deposited in the detector by fluorescence photons (ideally this is resolved by the fitting procedure of MAPS as described in Section 2). There may also be some signal as a result of elements in the medium in which the cells were prepared. The inhomogeneous background (see, e.g., the

K channel in Fig. 1) in many of the elemental maps introduces challenges for cell identification and for generating statistics on elemental content of various cell types.

For this reason, we calculate separate background content estimates for each group and region. As previously described, we distinguish the local background,  $B_g$  ( $B_r$ ), for group  $g \in \mathcal{G}$  (region  $r \in \mathcal{R}$ ) from the global background,  $B$ , associated with the entire image. We define the local background  $B_g$  as the set of background pixels that are within a distance  $\Delta > 0$  of  $G_g$ , or

$$B_g \equiv \{(x, y) \in B : |x - \hat{x}| + |y - \hat{y}| \leq \Delta \text{ for some } (\hat{x}, \hat{y}) \in G_g\} \quad (1)$$

where we recall that the foreground is defined as  $F = \cup_{g \in \mathcal{G}} G_g$  and the background is defined as  $B = P \setminus F$ .

As shown in Fig. 3, a region  $R_r = \cup_{g \in \mathcal{G}_r} (G_g \cup B_g)$  consists of a set of groups and their local backgrounds. The local background of a region is then defined in analogy to Equation (1) as the background outside of the region that is within a distance  $\Delta$  of the region, or

$$B_r \equiv \{(x, y) \in B \setminus R_r : |x - \hat{x}| + |y - \hat{y}| \leq \Delta \text{ for some } (\hat{x}, \hat{y}) \in R_r\}. \quad (2)$$

Although groups (as well as their backgrounds) may overlap, the regions are disjoint; however, the local backgrounds of different regions may overlap. Thus a region provides a convenient partitioning of the image into semi-independent structures, while groups allow for the modeling of overlapping cells. Initial groups, regions, and local backgrounds for the entire test dataset are illustrated in Fig. 3.

The primary purpose of obtaining local backgrounds is to adaptively estimate the local background content. For example,  $\mu_{er}$  denotes the mean (per-pixel) content of element  $e$  in the local background of region  $R_r$  and is defined as

$$\mu_{er} \equiv \frac{1}{|B_r|} c_e(B_r) = \frac{1}{|B_r|} \sum_{(x,y) \in B_r} c_e(x, y). \quad (3)$$

We similarly define the sample variance in the local background  $B_r$ :

$$\sigma_{er}^2 \equiv \frac{1}{|B_r| - 1} \sum_{(x,y) \in B_r} \left( c_e(x, y) - \frac{1}{|B_r|} c_e(B_r) \right)^2. \quad (4)$$

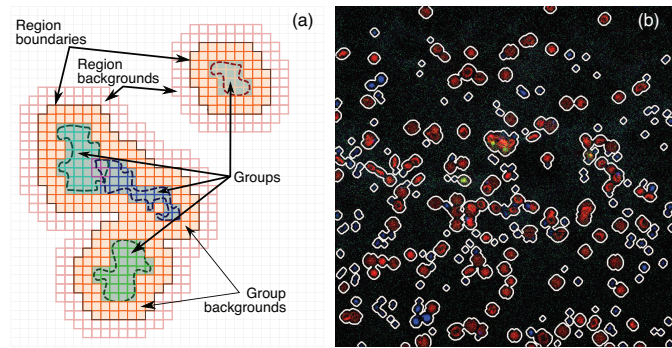


**Figure 3**  
(a) Illustration of groups, regions, and backgrounds. The innermost solid boundaries represent the union of groups, the next boundaries (black, orange fill) represent the regions, and the outermost boundaries (pink) represent the union of regions and region backgrounds. (b) Overlay showing distributions of Fe (red), Mn (green), Zn (blue), and the region boundaries (white).

**4.1.3. Content Computation for Groups.** Because we allow groups to overlap, it is necessary to apportion the content given by an elemental map among overlapping groups. A naïve way to distribute the content  $c_e(x, y)$  would be to split it equally among the groups that contain the pixel  $(x, y)$ . The approach that we take is to account for the relative abundance of the element with respect to the group’s type. For this we employ the representative means  $\mu_{et}$  introduced in Section 4.1.4.

Formally, we let  $\mathcal{G}_t(x, y) \subseteq \mathcal{G}$  denote the set of groups of type  $t \in \mathcal{T}$  that contain pixel  $(x, y)$ . A single group of type  $t$  containing  $(x, y)$  is thus assigned the fraction of content

$$f_{et}(x, y) = \frac{\mu_{et}}{\sum_{t' \in \mathcal{T}} |\mathcal{G}_{t'}(x, y)| \mu_{et'}}. \quad (5)$$

By construction, the content from an elemental map is preserved: summing over all groups containing  $(x, y)$  yields the elemental map content  $c_e(x, y)$ . Taking into account the background’s contribution and using this weighting, we define the assigned content of element  $e \in \mathcal{E}$  for group  $g \in \mathcal{G}$  of type  $t \in \mathcal{T}$  by

$$c_{egt} = \sum_{(x,y) \in G_g} f_{et}(x, y) (c_e(x, y) - \mu_{er}), \quad (6)$$

where  $r \in \mathcal{R}$  denotes the region that group  $G_g$  belongs to.

**4.1.4. Representative Cell Elemental Distributions.** For the subsequent procedures we require statistics of the content of each type of cell to broadly characterize the types of cells.

In the current approach, we represent the distribution of the total elemental content in a cell as a truncated (imposing non-negativity) Gaussian. Although other distributions can be used in our framework, we focus on Gaussians here to illustrate the method based on a small number of distributional parameters. In particular, if we assume that the contents for cells of different types and elements are independent, we need only to specify means and variances ( $\mu_{et}, \sigma_{et}^2$ ) for all  $e \in \mathcal{E}$  and  $t \in \mathcal{T}$ .

If such information is unavailable, it can be estimated by using a small number of expert hand-selected cells, particularly those that are well-separated from other cells in this particular example. Given a collection  $\mathcal{G}'(t)$  of hand-selected groups corresponding to cells of type  $t$ , we can use the sample mean

$$\hat{\mu}_{et} = \frac{1}{|\mathcal{G}'(t)|} \sum_{g \in \mathcal{G}'(t)} c_e(G_g), \quad (7)$$

and sample variance

$$\hat{\sigma}_{et}^2 = \frac{1}{|\mathcal{G}'(t)| - 1} \sum_{g \in \mathcal{G}'(t)} (c_e(G_g) - \hat{\mu}_{et})^2, \quad (8)$$

as estimates for  $\mu_{et}$  and  $\sigma_{et}^2$ , respectively.

## 4.2. Estimation of Group Configuration

The image segmentation in Section 4.1 is used to provide an initial group configuration (i.e., numbers and areas of groups). However, two drawbacks prevent this configuration from serving as putative cell areas: (1) only a single trace element for each cell type is taken into account, whereas cells are usually represented with multiple elements in XFM datasets; and (2) overlapping cells of the same type are not taken into account.

We now introduce an iterative procedure for adjusting this initial group configuration to a more realistic configuration. In each

iteration, the current configuration is updated to better match the region content with respect to the representative cell contents (from Section 4.1.4). We use a generalized likelihood ratio (GLR) test to determine whether such an update would improve the configuration for region  $R_r$ . This GLR test is formulated as (Wasserman, 2003)

$$\frac{\max_{\Theta_0} \mathcal{L}(H_0|c_r)}{\max_{\Theta_0^C} \mathcal{L}(H'|c_r)}. \quad (9)$$

The null hypothesis parameter space  $\Theta_0 = \{H_0\}$  has the current group configuration as its only hypothesis; the complementary parameter space  $\Theta_0^C$  has alternative hypotheses with reduced numbers of groups. We need only to consider alternative hypotheses with fewer groups  $|\mathcal{G}'| < |\mathcal{G}_r|$  (Wu & Nevatia, 2009) because of the over-segmentation discussed in Section 4.1.

Even if we only reduce the number of groups, testing all possible configurations is still prohibitive. To make this GLR test computationally tractable, we limit the parameter space  $\Theta_0^C$  to alternative hypotheses of exactly  $|\mathcal{G}_r| - 1$  groups, either through merging two groups  $g, g' \in \mathcal{G}_r$  (forming a new group from  $G_g \cup G_{g'}$ ) or deleting a group  $g \in \mathcal{G}_r$ .

The data here are the elemental content  $c_r = (c_{re})$  of all pixels in region  $R_r$ . Assuming the contents of groups in a region are independent, we can cast  $c_r$  as the sum of the contents ( $c_g = (c_{egt})$ ) in the groups  $g \in \mathcal{G}_r$  and the contents ( $c_{br} = (c_{ebr})$ ) in the respective local backgrounds  $\cup_{g \in \mathcal{G}_r} B_g$ . Formally, for all  $e \in \mathcal{E}$  we have

$$c_{re} = \sum_{(x,y) \in \{G_g; g \in \mathcal{G}_r\}} c_e(x, y) = c_{ebr} + \sum_{g \in \mathcal{G}_r} c_{egt}, \quad (10)$$

where  $c_{egt}$  is defined in Equation (6). The likelihood of our null hypothesis is thus evaluated as

$$\mathcal{L}(H_0|c_r) = \left( \prod_{g \in \mathcal{G}_r} \mathcal{L}(H_0|c_g) \right) \mathcal{L}(H_0|c_{br}). \quad (11)$$

The mean and variance of element  $e$  for group  $g$  (of type  $t$ ) in region  $R_r$  are defined by

$$\tilde{\mu}_{egr} = \mu_{er} |G_g| + \hat{\mu}_{et} \text{ and } \tilde{\sigma}_{egr}^2 = \sigma_{er}^2 |G_g| + \hat{\sigma}_{et}^2,$$

where  $\hat{\mu}_{et}$  and  $\hat{\sigma}_{et}^2$  are defined in Equation (7) and Equation (8). The likelihood  $\mathcal{L}$  of group  $g$  is

$$\mathcal{L}(H_0|c_g) = \left( \prod_{e \in \mathcal{E}} 2\pi \tilde{\sigma}_{egr}^2 \right)^{-\frac{1}{2}} \exp \left( -\frac{1}{2} \sum_{e \in \mathcal{E}} \frac{(c_{egt} - \tilde{\mu}_{egr})^2}{\tilde{\sigma}_{egr}^2} \right). \quad (12)$$

The likelihood of the background is defined similarly, with the background mean and variance of element  $e$  defined by

$$\tilde{\mu}_{ebr} = \mu_{er} \left| \bigcup_{g \in \mathcal{G}_r} B_g \right| \text{ and } \tilde{\sigma}_{ebr}^2 = \sigma_{er}^2 \left| \bigcup_{g \in \mathcal{G}_r} B_g \right|.$$

The likelihood of an alternative hypothesis  $H'$  is evaluated similarly to the null hypothesis in Equation (11). In the merging and deleting operations, we now need only to modify the appropriate terms corresponding to the configuration differences between  $H_0$  and  $H'$ :

- *Merging.* If  $H'$  corresponds to merging adjacent groups  $(g, g')$ , by convention the resulting group inherits the type  $t$

from the first group  $g$  (we also consider the pair  $(g', g)$ ). The new group has content computed by using the pixels  $G_g \cup G_{g'}$  in Equation (6). The updated means and variances for the new group  $g''$  are given by

$$\tilde{\mu}_{eg''r} = \mu_{er} |G_{g'} \cup G_g| + \hat{\mu}_{et} \text{ and } \tilde{\sigma}_{eg''r}^2 = \sigma_{er}^2 |G_{g'} \cup G_g| + \hat{\sigma}_{et}^2.$$

- **Deleting.** If  $H'$  corresponds to deleting group  $g$ , then we expand the background with all pixels only in group  $g$ . Those pixels are

$$G_g^* \equiv \{(x, y) \in G_g : \forall g' \in \mathcal{G}_r \setminus \{g\}, (x, y) \notin G_{g'}\}. \quad (13)$$

In the evaluation of joint likelihood, we drop the term with respect to  $c_g$  and update background means  $\tilde{\mu}_{eb'r}$  and variances  $\tilde{\sigma}_{eb'r}^2$  as

$$\tilde{\mu}_{eb'r} = \mu_{er} \left| \bigcup_{g \in \mathcal{G}_r} B_g \bigcup_{g \in \mathcal{G}_r} G_g^* \right| \text{ and } \tilde{\sigma}_{eb'r}^2 = \sigma_{er}^2 \left| \bigcup_{g \in \mathcal{G}_r} B_g \bigcup_{g \in \mathcal{G}_r} G_g^* \right|.$$

An example of how merging and deleting operations update the group configuration in a region is shown in Fig. 4.2. The outcome of this procedure (summarized in Procedure 2) is a group configuration that better describes the elemental content in every region.

**Procedure 2:** Estimation of group configurations (see Section 4.2).

Given regions  $\mathcal{R}$ , groups  $\mathcal{G}$ , elemental content  $c_r$ , and mean and variance of elemental content (e.g., from Equation (7)-Equation (8));

**for all regions  $r \in \mathcal{R}$  do**

**repeat**

Set NumRegChanged = 0;  
 Evaluate null hypothesis  $\mathcal{L}(H_0|c_r)$ ;  
 Find  $\mathcal{L}(H'|c_r) := \max \mathcal{L}(H|c_r)$  over  $H \in \Theta_0^c$ ;  
**if  $\mathcal{L}(H'|c_r) > \mathcal{L}(H_0|c_r)$  then**  
 NumRegChanged = 1;  
 Update  $\mathcal{G}_r$  according to  $H'$ ;

**until NumRegChanged = 0;**

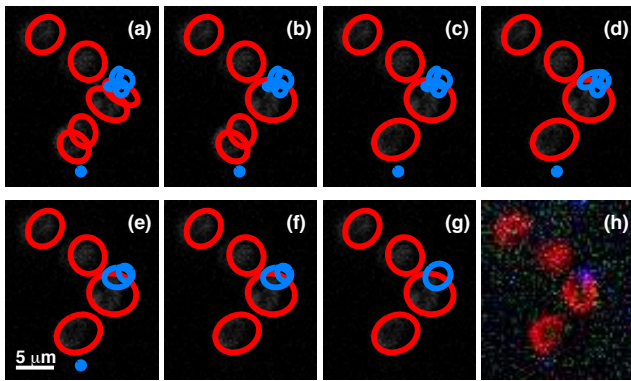


**Figure 4**

Example of the progress of group merging and deleting operations. (a) Initial configuration; (b),(c) merging two red blood cell groups; (d),(e),(g) merging two yeast cell groups; (f) deleting a yeast cell group. The overlay of Mn (green), Fe (red), and Zn (blue) elemental maps (h) shows that this area contains four red blood cells and one yeast cell, which overlaps one of the red blood cells. The end configuration in (g) shows that the estimation procedure identifies this configuration correctly. Group boundaries are shown as ellipses for illustration only; all operations are based on taking the union of pixels.

### 4.3. Optimization of Group Boundaries

The goal of our third procedure is to refine the area and location of each group so that the final shape and location best matches the elemental content for a particular type of cell to the given representative elemental content; see, for example Equation (7) and Equation (8). We formulate this problem as an optimization problem and develop a gradient-sampling (Burke *et al.*, 2005) Gauss-Newton approach to solve it.

Previous approaches to this problem include region-growing methodologies by active contour (Chan & Vese, 2001), level sets (Caselles *et al.*, 1995; Malladi *et al.*, 1995), and snake (Kass *et al.*, 1988). Our technique also builds on the inside-outside model described in (Amit, 2002). Our approach differs from these techniques in that we focus on growing the inside region with multiple intensity channels taken into account simultaneously, and we use gradient sampling to approximate the steepest descent directions of overlapping groups.

Our partition of the image into regions allows us to treat the optimization over each region independently; in the remainder of this section we describe the optimization over a single region  $R_r$ .

The unknown variables in the optimization problem are the parameters that describe the shape and location of the boundary of each group. In our experiments we parameterized the boundaries using Daubechies wavelets (Daubechies, 1992) truncated at level  $d$ ,  $\{\psi_k(\tau) : k = 0, \dots, d\}$ , where  $\tau \in [0, 1]$ . The boundary of a group  $g \in \mathcal{G}_r$  is parameterized as  $\theta_g(\tau) = (\theta_{gx}(\tau), \theta_{gy}(\tau))$  for  $x, y$  coordinates defined by wavelet coefficients  $u_{gk} = (u_{gkx}, u_{gky})$  as

$$\theta_g(\tau) = \sum_{k=0}^d u_{gk} \psi_k(\tau), \quad \text{for } \tau \in [0, 1]. \quad (14)$$

As a result, the unknowns in our optimization problems are the wavelet coefficients  $u = (u_{g0}, \dots, u_{gd})_{g \in \mathcal{G}_r}$ . In our experiments, these coefficients are initialized by fitting a minimum-area ellipse to each group generated in the previous step; see Section 4.2.

The objective function has two components: a proximal-point term that regularizes the objective and a data component that penalizes deviation of the group's elemental content from typical elemental cell content. The proximal-point term is  $\|u - u\|_\Lambda^2$ , where  $u$  is the initial parameterization (e.g., generated from a minimum-area ellipse). We use the squared, scaled  $\ell_2$ -norm  $\|w\|_\Lambda^2 = w^T \Lambda w$ , where  $\Lambda = \text{diag}(\lambda_i)$  is a diagonal scaling matrix with  $1/\lambda_i$  as the variance of component  $i$  of  $u$ , which accounts for the different scales of wavelet coefficients from different levels  $k = 0, \dots, d$ .

The data objective penalizes violation of typical elemental content. For every cell type  $t \in \mathcal{T}$  and element  $e \in \mathcal{E}$ , we define bounds  $(L, U)$  that take the region background into account. In our experiments, we use bounds based on being within one standard deviation of the mean elemental content or

$$U_{ert} = \mu_{et} + \sigma_{et} + \mu_{er} \text{ and } L_{ert} = \mu_{et} - \sigma_{et} + \mu_{er}.$$

Given these typical elemental bounds, we define the data objective for group  $g \in \mathcal{G}_r$  (of type  $t \in \mathcal{T}$ ) and element  $e \in \mathcal{E}$  as

$$h_e(c_e(u_g)) = \begin{cases} \frac{1}{2}(c_e(u_g) - U_{ert})^2 & \text{if } c_e(u_g) \geq U_{ert}, \\ 0 & \text{if } L_{ert} < c_e(u_g) < U_{ert}, \\ \frac{1}{2}(c_e(u_g) - L_{ert})^2 & \text{if } c_e(u_g) \leq L_{ert}, \end{cases} \quad (15)$$

where  $c_e(u_g) = c_{egt}$  is the assigned elemental content of the group  $G_g$  defined by the wavelet parameters  $u_g$ . The group's area can be

defined by an inverse wavelet transform. Summing the data objective over all elements, we define the region objective

$$J_r(u) = \sum_{g \in G_r} \sum_{e \in \mathcal{E}} h_e(c_e(u_g)) + \frac{\rho}{2} \|u - u\|_{\lambda}^2, \quad (16)$$

where  $\rho$  is a predefined parameter regularizing between the data term and the proximal-point term. The function  $J_r(u)$  is in general nonsmooth (due to the pixellation effect), and we therefore employ gradient sampling to approximate the steepest descent direction. We accelerate the steepest descent step with a Gauss-Newton procedure that exploits the fact that we know the Hessian,  $\rho\Lambda$ , of the second term. We terminate our optimization if the data objective becomes zero or when we reach an iteration limit.

#### 4.4. Optimality Test and Local Pixel Refinement

In this section, we describe an optimality test for evaluating the local optimality of group boundaries obtained using the procedure in Section 4.3. We also propose a procedure that locally refines boundary pixels on groups that do not satisfy this optimality test.

For a given group  $G_g$ , we define its inside boundary  $N_g^-$  and outside boundary  $N_g^+$  as

$$\begin{aligned} N_g^- &\equiv \{(x, y) \in G_g : \exists (x', y') \in B_g, \text{ and } \|(x, y) - (x', y')\|_1 = 1\}, \\ N_g^+ &\equiv \{(x, y) \in B_g : \exists (x', y') \in G_g, \text{ and } \|(x, y) - (x', y')\|_1 = 1\}. \end{aligned}$$

We also denote the updated objective  $J_r(u_g)$  as  $J_r(G_g)$  for the group of pixels  $G_g$ . We then define the following optimality test based on  $G_g$ ,  $N_g^+$ , and  $N_g^-$ :

**Optimality Test 1**  $G_g$  is said to have a locally optimal boundary if adding or deleting a single pixel does not improve  $J_r$ , that is, if  $J_r(G_g) \leq J_r(G_g \cup \{(x, y)\})$  for all  $(x, y) \in N_g^+$  and  $J_r(G_g) \leq J_r(G_g \setminus \{(x, y)\})$  for all  $(x, y) \in N_g^-$ .

If  $G_g$  does not satisfy this test, then we apply the local pixel refinement procedure (Procedure 3) to modify the boundary pixels of  $G_g$ . This procedure changes only one pixel at a time and repeats only *MaxIt* iterations. We employ this procedure for groups whose elemental contents are not within the range of  $[L_{err}, U_{err}]$  for at least one  $e \in \mathcal{E}$ , and we keep the *MaxIt* small (set to 5 in our experiments) so that the resulting  $G_g$  still maintains an approximately elliptic shape, as discussed in Section 4.1.1. This refinement procedure works for groups that are not overlapping with others because we have access to the exact  $J_r$  in the process of changing boundary pixels.

#### Procedure 3: Local pixel refinement (see Section 4.4).

Given pixel sets  $G_g$ ,  $N_g^-$ , and  $N_g^+$ ;

**for**  $iter < MaxIt$  **do**

    Let  $(x^+, y^+) = \operatorname{argmin}_{(x, y) \in N_g^+} J_r(G_g \cup \{(x, y)\})$

    and set  $J_r^+ = J_r(G_g \cup \{(x^+, y^+)\})$ ;

    Let  $(x^-, y^-) = \operatorname{argmin}_{(x, y) \in N_g^-} J_r(G_g \setminus \{(x, y)\})$

    and set  $J_r^- = J_r(G_g \setminus \{(x^-, y^-)\})$ ;

**if**  $J_r(G_g) \leq \min(J_r^+, J_r^-)$  **then**

        | Locally optimal: return;

**else if**  $J_r^- < J_r^+$  **then**

        | Remove pixel  $(x^-, y^-)$  from  $G_g$ ;

**else**

        | Add pixel  $(x^+, y^+)$  to  $G_g$ ;

    iter = iter+1;

## 5. Results

In this section, we present the results obtained from applying our approach to the test data set described in Section 2. The key metric of success is how well the elemental distributions of the identified cell populations match their corresponding known elemental distributions. We evaluate the resulting cell populations based on the elemental distributions of each cell's characteristic elements and multiple elements of well-measurable quantities (e.g., yeast cells contain P, K, Zn, etc.). In addition, we are interested in how different the elemental contents from identified cell populations comparing with those from the hand-drawn ROIs, especially if these ROIs are informative enough for identifying the entire cell population. As a byproduct, we also evaluate how well the background estimation works. We expect contents of well-measurable elements in given cell populations to be well above the estimated background derived from neighboring background pixels (Section 4.1.2) in their respective cell populations.

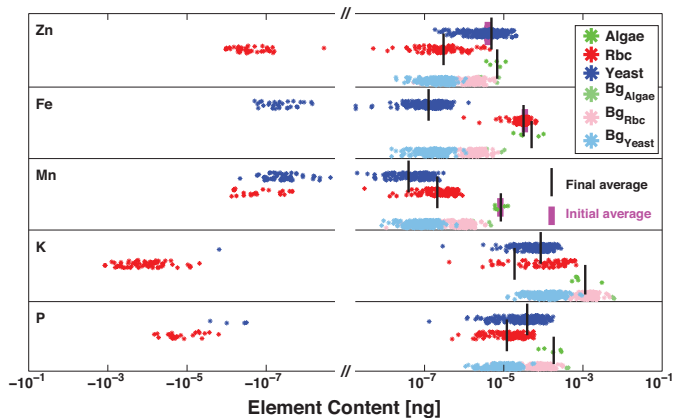


**Figure 5**

P, K, Mn, Fe, Zn content distributions of identified algae (green), yeast (blue), and red blood (red) cells. The light blue, pink, and light green points indicate the estimated background (Bg) contents of the respective cell areas. The horizontal axis (log scale) shows net elemental content, and the points are distributed randomly within bounds in the vertical direction in order to provide separation. The magenta and black lines show, respectively, the initialized means from hand-drawn regions of interest, and the means of the actual cell populations in the characteristic elements. As expected, the cells tend to have high elemental content in their characteristic elements: red blood cells have high Fe content, and yeast cells contain significant amounts of P and Zn. Some elements can show negative content for some cells (the K channel in red blood cells, for example); this is because of the need to subtract substrate and background signals from the raw elemental content to calculate the actual elemental content for a given cell. In case the signal is close to zero, the statistical nature of the collected signal can lead to negative numbers when two nearly equal signals are subtracted.

In Fig. 5, we show color-coded elemental distributions (P, K, Mn, Fe, Zn) for the three cell types. These elemental distributions are the net contents after removal of estimated background. We also include an additional row showing the estimated background distributions. We observe the following:

1. If a cell population contains well measurable amounts of specific elements, then the corresponding net contents (after removing background using neighbor background pixels) are well above zero. For example, the characteristic elements (Mn, Fe and Zn) are distinctly high in their respective cell populations; yeast cells also show high contents in P and K simultaneously. For those elements whose contents in cells are close to detection limits, their net content distributions

can have both positive and negative values. This is because (1) the statistical nature of the collected signal can lead to negative numbers when two nearly equal signals are subtracted; (2) Some of these elements contain “halo” regions, if the identified cells do not contain large quantity of these elements and they are inside of these regions (e.g., K content in red blood cells), we can obtain negative net contents.

- The distances between the magenta and black lines show how much the initial guesses from a few hand-drawn ROIs differ from the means of the cell populations determined by our method. The mean contents from the identified cell populations (>100 cells) are within 20% ranges compared with the mean contents from hand-drawn ROIs, which include no more than 10 cells. This indicates that the cell populations in our dataset have consistent elemental contents, especially in their respective characteristic elements.

To summarize, we observe that all identified cells have significant contents that match their respective biological expectations. These elemental contents are different from the mean contents of the hand-drawn ROIs by about 20%. Furthermore, our background estimation works well for elements with well-measurable amounts in given cell populations.

## 6. Discussion and Validation

The cell identification results we report in Section 5 use the sum of the four detector measurements, where each detector segment records the fluorescence signal from a slightly different viewing angle. This can lead to slight variations in calculated elemental concentration because of variations in scattering background and absorption of fluorescence signal along the viewing path. To validate that the identified cell areas do contain cells, we applied this approach to each elemental concentration map separately and compared the elemental distributions of all resulting cell populations. Our assumption is that if an area contains actual cells, all four detectors will measure significant elemental signals from it. In this case, if our approach identifies similar cells from all four individual measurements and the sum of them, this identification agreement provides evidence that our approach finds cells correctly.

Figure 6 shows the elemental content from the resulting red blood and yeast cells (there are only 5 algae cells). These scatterplots show that the Fe distributions of resulting red blood cells and the Zn distributions of resulting yeast cells are similar. An ANOVA test (Rice, 1995) determines that none of the five cell populations has statistically significant differences in elemental distribution. Hence we conclude that this identification approach using different measurements of the same sample recognizes similar elemental distributions of each resulting cell population.

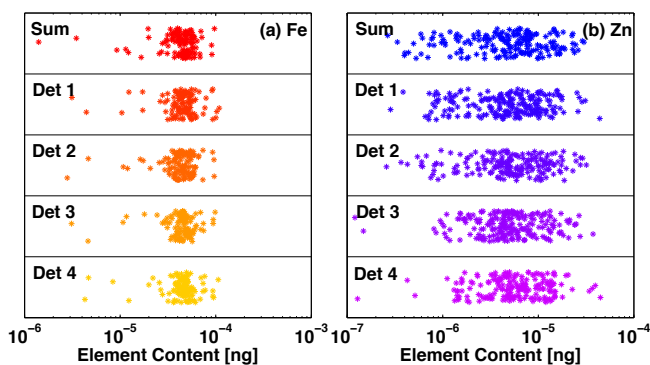


**Figure 6**

(a) Scatterplot of Fe distributions from red blood cells obtained using the separate detector segments as well as their sum. (b) Scatterplot of Zn distributions from yeast cells obtained using separate detector segments as well as their sum. The horizontal axis (log scale) shows element content in ng; in the vertical direction, points are distributed randomly within a bound for separation. This figure demonstrates that elemental contents obtained by separate analyses from the different detector segments are quite similar, adding confidence in the robustness of our results.

We also examined the dependence on the initial determination of foreground and background regions. In the preprocessing step, we divide pixels into foreground and background components based on the thresholding pixel intensity in the respective elemental maps. We evaluate the robustness of our approach by varying the threshold  $\pm 20\%$ . This thresholding variation changes the initial group configurations. We would like to evaluate whether the resulting cell populations using all three thresholds have similar numbers of cells and similar elemental content distributions. Significantly different elemental distributions indicate this approach may be sensitive to this range of threshold variation.

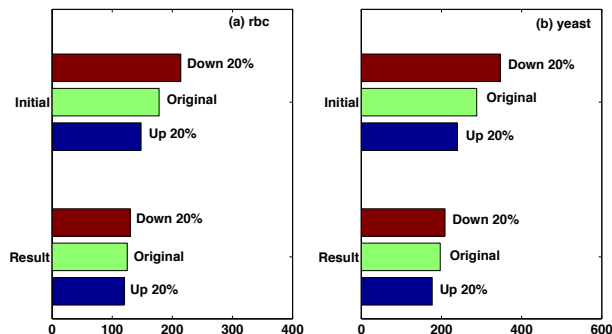


**Figure 7**

Test of the total number of red blood cells (a) and yeast cells (b) identified as the initial choice for elemental thresholding is changed over a 20% range. Of course the initial threshold choice produces large changes in the number of cells identified in the first pass of our approach, but this dependence on initial parameters is greatly reduced at the end of our analysis sequence.

The up/down thresholding changes the number of initial groups (“Initial” in Fig. 7) by 15–20%, whereas the numbers of cells among all resulting cell populations (“Result” in Fig. 7) differ only by 5–8%. For example, the preprocessing procedure obtains 288 initial yeast cell groups using the original threshold, and there are 197 yeast cells in the resulting cell population; using downthresholding, the preprocessing obtains 347 initial (a 20% difference) and 209

final (a 6% difference) yeast cell groups. These results illustrate that our final cell populations are relatively insensitive to the different thresholding, the final results, change only by  $\pm 8\%$ .

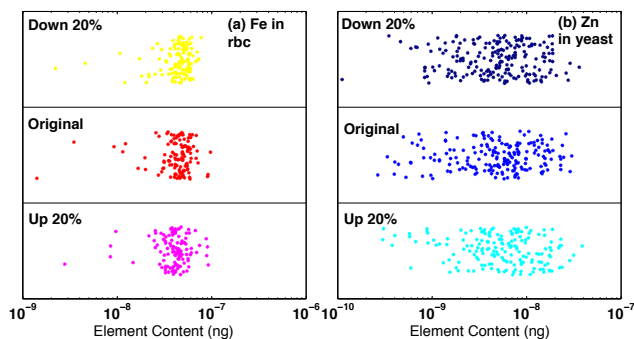


**Figure 8** Scatterplots showing (a) Fe distributions in red blood cell populations and (b) Zn distributions in yeast cell populations resulting from three different initial elemental thresholding choices. The similarity of results shows that the results obtained are robust against changes in initial parameters.

We also compare the elemental contents of cell populations resulting from the three different initial threshold choices. The scatterplots in Fig. 8 show that both the Zn distributions of the resulting yeast cell populations and Fe distributions of the resulting red blood cells are insensitive to the different thresholding. Furthermore, we found no significant difference in the means of all three Zn (and Fe) distributions using a one-way ANOVA test.

These results show that our approach is able to estimate elemental content of cell populations very well, with final results being insensitive to modest changes in initial input parameters.

## 7. Conclusion and Future Work

We describe here an approach for identifying cells of complex configurations (including heavily overlapping cells) in multi-dimensional XFM datasets. Without explicit expert knowledge and training using manual annotation, we demonstrate that this approach can differentiate multiple cell types using trace element contents. The generalized likelihood ratio test is robust in determining cell configurations using initial putative groups generated by using various elemental content thresholds. Furthermore, our approach shows consistent performance in processing regions with overlapping structures, where it is difficult to obtain reliable cell identification manually, given the volume and complexity of current microscopy data.

Extensions we plan to integrate into this methodology include modeling the cell size, adapting the covariance matrix according to the cell size, and making this approach iterative so that the result from the pixel refinement is fed back to the estimation of group configurations to further improve the identification. We also intend to study more complicated cases, including cells with arbitrary shapes, sizes, and heterogeneous (i.e., non-Gaussian) elemental content distributions, and to analyze full XFM spectra. In addition, we are interested in developing metrics to measure quantitatively the performance of this type of unsupervised approach.

**Acknowledgments.** This work was supported by the U.S. Department of Energy, Office of Science, Advanced Scientific Computing Research, and Basic Energy Sciences program [DE-AC02-

06CH11357] and Argonne National Laboratory [project 2011-149-NO 9164]. We thank Qiaoling Jin and Sophie-Charlotte Gleber for helpful suggestions.

## References

- Al-Kofahi, Y., Lassoued, W., Lee, W. & Roysam, B. (2010). *IEEE Transactions on Biomedical Engineering*, **57**(4), 841–852.
- Amit, Y. (2002). *2D Object Detection and Recognition: Models, Algorithms, and Networks*. Cambridge, MA: MIT Press.
- Arteta, C., Lempitsky, V., Noble, J. A. & Zisserman, A. (2012). In *Proceedings of the 15th International Conference on Medical Image Computing and Computer-Assisted Intervention (MICCAI12)*, pp. 348–356. Berlin: Springer-Verlag.
- Aydin, Z., Murray, J., Waterston, R. & Noble, W. (2010). *BMC Bioinformatics*, **11**(1), 1–13.
- Bergeest, J.-P. & Rohr, K. (2011). *LNCS*, **6891**, 645–652.
- Bergeest, J.-P. & Rohr, K. (2012). *Medical Image Analysis*, **16**(7), 1436–1444.
- Burke, J. V., Lewis, A. S. & Overton, M. L. (2005). *SIAM Journal on Optimization*, **15**(3), 751–779.
- Caselles, V., Kimmel, R. & Sapiro, G. (1995). *International Journal of Computer Vision*, **22**, 61–79.
- Chan, T. & Vese, L. (2001). *IEEE Transactions on Image Processing*, **10**(2), 266–277.
- Cortés, L. & Amit, Y. (2008). *IEEE Transactions on Pattern Analysis and Machine Intelligence*, **30**(11), 1998–2010.
- Daubechies, I. (1992). *Ten Lectures on Wavelets*. CBMS-NSF Regional Conference Series in Applied Mathematics. Philadelphia, PA: SIAM.
- Dhillon, I., Guan, Y. & Kulis, B. (2007). *IEEE Transactions on Pattern Analysis and Machine Intelligence*, **29**(11), 1944–1957.
- Dismukes, G. C. (1986). *Photochemistry and Photobiology*, **43**(1), 99–115.
- Good, N. E., Winget, G. D., Winter, W., Connolly, T. N., Izawa, S. & Singh, R. M. (1966). *Biochemistry*, **5**(2), 467–477.
- Gorman, D. S. & Levine, R. P. (1965). *Proceedings of the National Academy of Sciences of the United States of America*, **54**(6), 1665–1669.
- Hawkins, W. W., Speck, E. & Leonard, V. G. (1954). *Blood*, **9**(10), 999–1007.
- Kass, M., Witkin, A. & Terzopoulos, D. (1988). *International Journal of Computer Vision*, **1**(4), 321–331.
- Kasson, P. M., Huppa, J. B., Davis, M. M. & Brunger, A. T. (2005). *Bioinformatics*, **21**(19), 3778–3786.
- Kirz, J. (1980). In *Ultrasoft X-ray Microscopy: Its Application to Biological and Physical Sciences*, edited by D. F. Parsons, Annals of the New York Academy of Sciences, pp. 273–287. New York.
- Krause, M. O. (1979). *Journal of Physical and Chemical Reference Data*, **8**, 307–327.
- Lerotic, M., Jacobsen, C., Gillow, J., Francis, A., Wirick, S., Vogt, S. & Maser, J. (2005). *Journal of Electron Spectroscopy and Related Phenomena*, **144–147**, 1137–1143.
- Lerotic, M., Jacobsen, C., Schäfer, T. & Vogt, S. (2004). *Ultramicroscopy*, **100**(1–2), 35–57.
- Lin, G., Adiga, U., Olson, K., Guzowski, J. F., Barnes, C. A. & Roysam, B. (2003). *Cytometry Part A*, **56A**(1), 23–36.
- Ljosa, V. & Carpenter, A. E. (2009). *PLoS Computational Biology*, **5**(12), e1000603.
- Lundblad, V. & Struhl, K. (2001). In *Current Protocols in Molecular Biology*, pp. 13.0.1–13.0.4. Hoboken, NJ: John Wiley & Sons.
- Malladi, R., Sethian, J. & Vemuri, B. (1995). *IEEE Transactions on Pattern Analysis and Machine Intelligence*, **17**(2), 158–175.
- McCullough, D. P., Gudla, P. R., Harris, B. S., Collins, J. A., Meaburn, K. J., Nakaya, M. A., Yamaguchi, T. P., Misteli, T. & Lockett, S. J. (2008). *IEEE Transactions on Medical Imaging*, **27**(5), 723–734.
- Paunesku, T., Vogt, S., Maser, J., Lai, B. & Woloschak, G. (2006). *Journal of Cellular Biochemistry*, **99**, 1489–1502.
- Plaza, A., Martinez, P., Perez, R. & Plaza, J. (2004). *Pattern Recognition*, **37**(6), 1097–1116.
- Rice, J. A. (1995). *Mathematical Statistics and Data Analysis*. Belmont, CA: Duxbury Press, 2nd ed.
- Russell, C., Metaxas, D., Restif, C. & Torr, P. (2007). In *2007 IEEE International Conference on Computer Vision*, pp. 2362–2369.
- Swedlow, J. R., Goldberg, I. G. & Eliceiri, K. W. (2009). *Annual Review of Biophysics*, **38**(1), 327–346.

- 
- Tao, C. Y., Hoyt, J. & Feng, Y. (2007). *Journal of Biomolecular Screening*, **12**(4), 490–496.
- Vogt, S. (2003). *Journal de Physique IV*, **104**, 635–638.
- Wang, M., Zhou, X., Li, F., Huckins, J., King, R. W. & Wong, S. T. C. (2007). *Bioinformatics*, **24**(1), 94–101.
- Wasserman, L. (2003). *All of Statistics: A Concise Course in Statistical Inference*. Springer.
- Wolz, R., Heckemann, R. A., Aljabar, P., Hajnal, J. V., Hammers, A., Lötjönen, J. & Rueckert, D. (2010). *NeuroImage*, **52**(1), 109–118.
- Wu, B. & Nevatia, R. (2009). *International Journal of Computer Vision*, **82**(2), 185–204.
- Yin, Z., Bise, R., Chen, M. & Kanade, T. (2010). In *ISBI*, pp. 125–128.

The submitted manuscript has been created by the University of Chicago as Operator of Argonne National Laboratory (“Argonne”) under Contract DE-AC02-06CH11357 with the U.S. Department of Energy. The U.S. Government retains for itself, and others acting on its behalf, a paid-up, nonexclusive, irrevocable worldwide license in said article to reproduce, prepare derivative works, distribute copies to the public, and perform publicly and display publicly, by or on behalf of the Government.